Journal of *Marine Science and Engineering*

MDPI

Article

Numerical Evaluation of Commingled Production Potential of Marine Multilayered Gas Hydrate Reservoirs Using Fractured Horizontal Wells and Thermal Fluid Injection

Shuaishuai Nie [1], Jiangfei Li [1,*], Ke Liu [1], Xiuping Zhong [2] and Yafei Wang [2]

[1] School of Petroleum Engineering, Hebei Petroleum University of Technology, Chengde 067000, China; niess20@mails.jlu.edu.cn (S.N.); lkcdpc@hotmail.com (K.L.)
[2] College of Construction Engineering, Jilin University, Changchun 130026, China; zhongxp17@mails.jlu.edu.cn (X.Z.); yfwang18@mails.jlu.edu.cn (Y.W.)
* Correspondence: lijiangfei@cdpc.edu.cn

Abstract: Multilayered reservoirs with coexisting free gas and hydrates are primary targets for commercialization, nevertheless, the extremely low permeability greatly limits their extraction efficiency. Herein, multilayer commingled production using horizontal wells stimulated by hydraulic fracturing and thermal fluid injection was proposed to enhance productivity, and the effects of key factors on co-production performance were numerically examined, with the reservoir located in the Shenhu Area as the geological background. The results indicated that due to severe interlayer contradictions, the stimulation capabilities of using fracturing or thermal fluid injection alone were limited, in particular, the extraction of hydrates severely lagged behind. However, their combination exhibited tantalizing productivity due to strengthened inter-well interaction. Reducing the fracture spacing was more effective than increasing fracture conductivity in shortening the production cycle, and intensive fractures with adequate flow capacity were suggested for gas enhancement and water control. When the fracture spacing was reduced from 30 to 5 m and the fracture conductivity increased from 10 to 100 D·cm, the horizontal section length for commercial production (average daily gas production of 50,000 m^3 and recovery ratio of 0.7) was reduced from 1758 to 146 m, which is lower than the on-site horizontal section length of 250–300 m. Therefore, the proposed development mode is promising for the commingled production of gas and hydrates.

Keywords: natural gas hydrate; commingled production; multilayer; horizontal well; stimulation technology

Citation: Nie, S.; Li, J.; Liu, K.; Zhong, X.; Wang, Y. Numerical Evaluation of Commingled Production Potential of Marine Multilayered Gas Hydrate Reservoirs Using Fractured Horizontal Wells and Thermal Fluid Injection. *J. Mar. Sci. Eng.* **2024**, *12*, 365. https://doi.org/10.3390/jmse12030365

Academic Editor: Dejan Brkić

Received: 5 February 2024
Revised: 17 February 2024
Accepted: 19 February 2024
Published: 21 February 2024

1. Introduction

Natural gas hydrate (NGH) is a cage-like crystallized compound consisting of gas (mainly CH_4) and water that is widespread in submarine sediments and permafrost regions [1]. The organic carbon content in naturally occurring NGH is estimated to be about 10^4 billion tons, approximately one-third of the world's total. As a result, NGH is widely recognized as the ideal new clean energy resource for the 21st century [2].

Gas recovery from NGH faces enormous challenges due to the harsh environment, complex phase behavior, and potential geo-environmental risks. Currently, only 10 production trials have been carried out at the Mallik site in Canada [3], the North Slope of Alaska [4], the Nankai Trough [5], the Qilian Mountains [6], and the Shenhu Area [7]. The production trials in the Shenhu Area especially demonstrated the feasibility of gas extraction from oceanic clayey-silty sediments. This challenging storage environment contains more than 90% of the world's NGH resources and is generally considered the most difficult to extract due to its low effective permeability [8]. However, since there are three sublayers, that is, the hydrate-bearing layer (HBL), three-phase layer (TPL), and free gas layer (FGL), and the use of horizontal well technology, the productivity is the

highest. Additionally, such multilayered reservoirs with coexisting NGH and free gas are quite prevalent and have been found at Blake Ridge [9], Green Canyon [10], and Offshore Oregon [11], and are, therefore, generally recognized as the "sweet spots" and primary targets for commercialization.

Recently, aiming for the commercialization of gas hydrates, various development modes have been raised, including the following: i. thermal stimulation to provide sufficient energy for hydrate dissociation, with heating methods including massless injection in the form of electrical or microwave heating [12,13], as well as thermal fluid injection (mainly hot water) in the form of single-well huff and puff [14] and injection-production well patterns [15]; ii. using horizontal wells to increase the drainage area, such as radially branched horizontal wells [16]; iii. implementing reservoir reconstruction such as enlarged permeable well walls [17] and hydraulic fracturing [18] to improve reservoir permeability; iv. injecting gases (mainly CO_2) that are more likely to form hydrates to replace CH_4 molecules in NGH cages [19]; v. injecting chemical inhibitors like brine to promote NGH dissociation [20]; vi. integrating multiple methods, such as combining fracturing and multi-well systems [21], and using thermal stimulation and chemical inhibitors [22]. Nevertheless, these studies mainly focus on the production dynamics of reservoirs with a single HBL, with few simulations exploring the commingled production of multilayers. Yu et al. (2021) found that the gas contribution of each sublayer was FGL, HBL, and TPL in descending order for a vertical well [23]. Subsequently, the exploitation dynamics of the horizontal well with multiple artificial fractures were further simulated, and the results indicated that horizontal fractures contributed more to productivity [24]. Ma et al. (2021) examined the influences of well location and found that deploying the horizontal section in the HBL was beneficial for long-term production [25]. Yin et al. (2022) suggested that the low permeability of the HBL inhibits pressure and temperature transfer, leading to inefficient hydrate decomposition [26]. Overall, the above studies preliminarily proved the feasibility of implementing multilayer co-production using horizontal wells. However, several crucial issues need further research: firstly, the capabilities of various means of stimulation like hot water injection and fracturing are poorly understood; secondly, the response mechanism of co-production dynamics to various stimulation factors is still unclear; and lastly, the commercial development potential of multilayer co-production has not yet been effectively assessed.

This study aims to investigate the above issues through simulations of commingled production in the multilayered reservoir located in the Shenhu Area. Firstly, co-production performance using horizontal wells stimulated by hydraulic fracturing and/or thermal fluid injection was compared, followed by the effects of fractured sublayers, fracture spacing, and fracture conductivity on co-production dynamics, including hydrate decomposition and gas–water production; and finally, through variance analysis and commercial potential evaluation, the optimal multilayer co-production plan was obtained. The findings of this study help to understand the peculiar multilayer co-production behavior and stimulation mechanism, as well as provide references for the implementation of reservoir stimulation and the design of co-production schemes. In addition, the proposed multilayer co-production with the combined stimulation of horizontal well fracturing and hot water injection offers an attractive development mode for this kind of low-permeability multilayered "sweet-spot" gas hydrate reservoir, which is conducive to promoting the industrialization process of marine-challenging hydrates.

2. Numerical Modeling

2.1. Geoengineering Background

The Shenhu Area, located in the South China Sea, is the main NGH-rich area in China. Since 2007, three gas hydrate geological surveys have been carried out, during which samples with a hydrate saturation of 20–48% and CH_4 content of more than 99.7% were recovered [27]. Recent research on the deposition system has demonstrated the coexistence of hydrate and free gas by analyzing geology and logging data [28].

2.2. Development Mode Design

Here, the multilayered reservoir with a seawater depth of 1225.23 m at the test site was taken as the research object, as shown in Figure 1. The target production layers are located at 207.8–297 mbsf. The thicknesses of the overlayer (OL) and underlayer (UL) were set to 30 m to accurately simulate the reservoir temperature and pressure evolution [29]. A three-spot well pattern was used with all horizontal sections extending along the Y-axis. Two depressurization wells were arranged at the top of the TPL for the co-production of free gas and NGH dissociation gas, while the middle injection well was deployed at the top of the HBL to maximize the hot water sweep area. Reservoir properties were assumed to be homogeneous in the horizontal since there is no available data for reference, and thus, only a 30 m horizontal well section was considered for simulation.

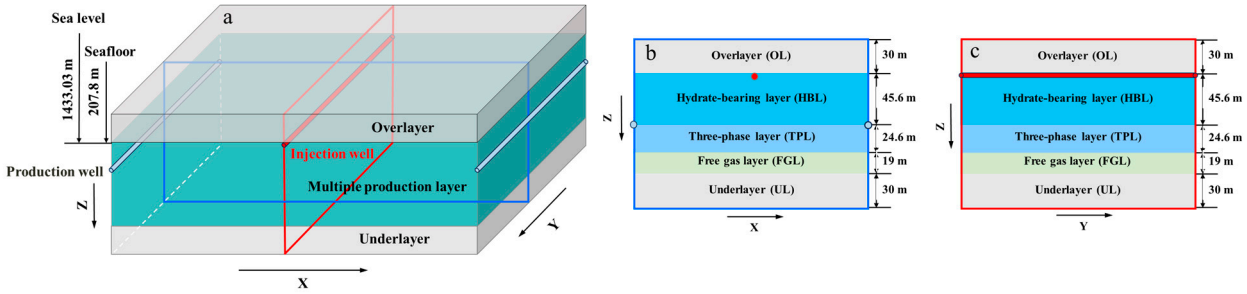

Figure 1. The three-spot horizontal well pattern in the multilayered gas hydrate reservoir: (**a**) 3D view, (**b**) X–Z, and (**c**)Y–Z cross-sections.

It was assumed that multiple vertical fractures were formed by segmental fracturing, as shown in Figure 2. The well spacing was set to 30 m for inter-well connectivity. To reveal the impact of fractured sublayers on co-production performance, three cases were considered, that is, fractured HBL (Figure 2a), fractured HBL and TPL (Figure 2b), and fractured HBL, TPL, and FGL (Figure 2c). In addition, the value of fracture spacing was set to four levels: 30, 15, 10, and 5 m, and thus, a 30 m horizontal section contained two, three, four, and seven fractures, respectively, as shown in Figure 2d–g.

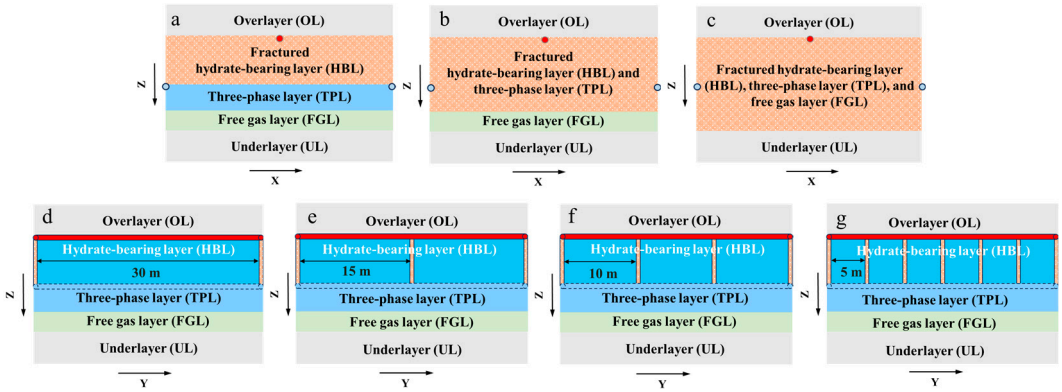

Figure 2. Different fractured sublayers at X–Z cross-section (**a**–**c**), and different fracture spacings at Y–Z cross-section (**d**–**g**).

2.3. Numerical Simulator

Several numerical simulators have been developed for NGH exploitation, such as CMG-STARS, Tough + Hydrate (T + H), and HydrResSim. Among them, T + H is preferred because of its powerful functions in mine scale simulation. Moreover, its accuracy has been fully examined [30] and thus was employed here.

NGH exploitation is accompanied by phase transition, as follows

$$CH_4 \cdot 5.75H_2O = CH_4 + 5.75H_2O \tag{1}$$

The mass and energy balances in each domain are expressed as [31]

$$\frac{d}{dt}\int_{V_n} M^\kappa dV = \int_{\Gamma_n} F^\kappa dV \cdot n d\Gamma + \int_{V_n} q^\kappa dV, \kappa \equiv m(CH_4), w(\text{water}), i(\text{inhibitor}), \theta(\text{heat}) \tag{2}$$

The mass accumulation term is given by

$$M^\kappa = \sum_{\beta=H,A,G,I} \phi\rho_\beta S_\beta X_\beta^\kappa,\ \beta \equiv H(\text{hydrate}),\ A(\text{aqueous}),\ G(\text{gaseous}),\ I(\text{ice}) \tag{3}$$

The energy accumulation term consists of the matrix energy, energies of all phases, and NGH dissociation activation energy, as follows

$$M^\theta = (1-\phi)\rho_{sed}C_{sed}T + \sum_{\beta=G,A,H,I} \phi\rho_\beta S_\beta U_\beta + E_{dis} \tag{4}$$

In the code, Darcy's law is employed, while taking into account the diffusion effect of the gaseous and multiphase fluid flow, and is described by

$$F_A^\kappa = -k\frac{k_{rA}\rho_A X_A^\kappa}{\mu_A}(\nabla P_A - \rho_A g) \tag{5}$$

$$F_G^\kappa = -k\frac{k_{rG}\rho_G X_G^\kappa}{\mu_G}\left(1 + \frac{\omega}{P_G}\right)(\nabla P_G - \rho_G g) \tag{6}$$

The relative permeabilities of the gaseous and aqueous are given by [32]

$$k_{rA} = \left(\frac{S_A - S_{irA}}{1 - S_{irA}}\right)^{n_A} \tag{7}$$

$$k_{rG} = \left(\frac{S_G - S_{irG}}{1 - S_{irA}}\right)^{n_G} \tag{8}$$

The aqueous pressure considering capillary pressure is expressed as

$$P_A = P_G + P_{cap} \tag{9}$$

The capillary pressure in the gas hydrate system is described by [33]

$$P_{cap} = -P_{thr}\left[\left(\frac{S_A - S_{irA}}{1 - S_{irA}}\right)^{-\frac{1}{\lambda}} - 1\right]^{1-\lambda} \tag{10}$$

The energy flux is expressed as

$$F^\theta = f_\sigma \sigma_0 \nabla T^4 - \left[\left(1 - \phi K_{sed} + \phi \sum_{\beta=G,A,H,I} S_\beta K_\beta\right)\right]\nabla T + \sum_{\beta=G,A} h_\beta F_\beta \tag{11}$$

The mass and energy source-sink terms are expressed as follows

$$q^\kappa = \sum_{\beta=G,A} X_\beta^\kappa q_\beta \tag{12}$$

$$q^\theta = q_d + \sum_{\beta=G,A} h_\beta q_\beta \tag{13}$$

2.4. Initial and Boundary Conditions

The pore seawater was assumed to be connected because of the open boundaries, and thus, the pore pressure gradient was calculated by

$$P_{por} = P_{atm} + \rho_{sw} g(h_0 + z) \quad (14)$$

In addition, the temperature field was initialized based on the following equation

$$T = T_{sf} + \Delta T \cdot z \quad (15)$$

Dirichlet boundary conditions were imposed at upper and lower boundaries, with constant pressures and temperatures there. Additionally, the porosity and intrinsic permeability of the OL and UL were not available, and are, therefore, presumed to be the same as those of the adjacent sublayers. Notably, the temperature–pressure transmission and fluid flow induced by OL and UL are greatly weakened because of the use of hydraulic fracturing and thermal fluid injection, making the impact of this simplification on the simulation results very limited. The model parameters are presented in Table 1.

Table 1. Model parameters.

Parameters	Value & Unit
Porosity of OL, HBL, TPL, FGL, and UL	0.373, 0.373, 0.346, 0.347, and 0.347
Intrinsic permeability of OL, HBL, TPL, FGL, and UL	2.38, 2.38, 6.63, 6.8, and 6.8 mD
Mean hydrate saturation in HBL and TPL	31% and 11.7%
Mean gas saturation in TPL and FGL	13.2% and 9.3%
Gas composition	CH_4 100%
Seawater salinity	0.03
Dry and wet thermal conductivity (all deposits)	1 and 3.1 W/m/K
Sediment density	2650 kg/m^3
Sediment specific heat	1000 J/K/kg
Production and injection pressure	3 and 16 MPa
Hot water temperature	60 °C
ρ_{sw}	1024 kg/m^3
T_{sf}	3.6 °C
ΔT	46 °C/km
P_{thr}	1×10^5 Pa
λ	0.45
n_A	3.50
n_G	3.50
S_{irA}	0.30
S_{irG}	0.03

2.5. Model Validation

A simulation was conducted on the unit-length horizontal section for model validation, and the simulation data are shown in Figure 3. As can be seen, 3312 m^3 of gas was recovered from the unit-length horizontal section over 30 days. This results in 861,400 m^3 of gas for a horizontal section length of 260 m, within the range of the on-site horizontal section length of 250–300 m [34], proving the accuracy of the model.

2.6. Simulation Scenarios

The co-production performances of four development modes were compared, that is, depressurization without stimulation (D), stimulation using fracturing (D+F) or thermal fluid injection (D+T), or both (D+T+F). Additionally, referring to the existing research, the fracture conductivity was set to 10–100 D·cm [21]. Ultimately, the factors examined include stimulation methods, fractured sublayers, fracture spacing, and fracture conductivity, with simulation scenarios presented in Table 2.

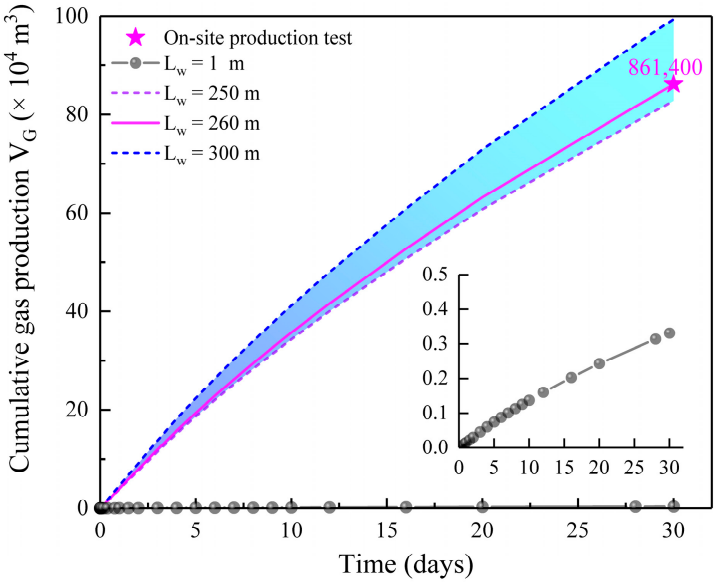

Figure 3. Model validation based on the on-site trail production data.

Table 2. Simulation scenarios.

Scenario No.	Development Mode	Fractured Sublayers	C_F (D·cm)	S_F (m)	Scenario No.	Development Mode	Fractured Sublayers	C_F (D·cm)	S_F (m)
01#	D	/	/	/	12#	D+T+F	HBL, TPL	25	15
02#	D+T	/	/	/	13#	D+T+F	HBL, TPL	25	10
03#	D+F	HBL	10	30	14#	D+T+F	HBL, TPL	25	5
04#	D+T+F	HBL	10	30	15#	D+T+F	HBL, TPL	50	30
05#	D+T+F	HBL, TPL	10	30	16#	D+T+F	HBL, TPL	50	15
06#	D+T+F	HBL, TPL, FGL	10	30	17#	D+T+F	HBL, TPL	50	10
07#	D+T+F	HBL, TPL	10	30	18#	D+T+F	HBL, TPL	50	5
08#	D+T+F	HBL, TPL	10	15	19#	D+T+F	HBL, TPL	100	30
09#	D+T+F	HBL, TPL	10	10	20#	D+T+F	HBL, TPL	100	15
10#	D+T+F	HBL, TPL	10	5	21#	D+T+F	HBL, TPL	100	10
11#	D+T+F	HBL, TPL	25	30	22#	D+T+F	HBL, TPL	100	5

3. Results and Discussion

3.1. Comparison of Different Development Modes

The co-production performance under different development modes was compared based on scenario numbers 01~04#.

3.1.1. NGH Dissociation

Figure 4 depicts the evolution of Q_R and R_D under different development modes. The Q_R in the D mode exhibited an initial sharp drop and a subsequent (~300 days) slow decrease. The mechanism for this is twofold: first, the NGH dissociation front gradually moved away from the wellbores (Figure 5a–c); and second, the reservoir temperature decreased significantly (Figure 6a–c) and cannot provide enough heat for hydrate dissociation. In addition, the hydrate around the middle horizontal well was barely decomposed because boundary water intrusion hinders pressure drop transmission [35,36]. Owing to the greater permeability and the critical steady state of the hydrates, a larger hydrate decomposition radius was observed in the TPL (Figure 5c). In the D+T mode, the improvement in Q_R was not significant as hot water injection and migration were suppressed by the HBL's low permeability (Figure 5d–f), and substantial hot water leakage into the OL can be observed in Figure 6d–f, resulting in only a 15% increase in the final R_D (Figure 4). In the D+F mode, the maximum Q_R was increased to 3974 m^3/d as rapid NGH dissociation occurred along fractures (Figure 5g–i), and the reservoir temperature dropped significantly due to the limited sensible heat (Figure 6g–i), resulting in a sharp decrease in Q_R [37]. At 1200 days,

the hydrates in the TPL were almost completely decomposed, whereas a substantial amount of hydrates was still reserved in the HBL (Figure 5i). Thus, the extraction efficiency of the HBL was still severely lagging even after fracturing. In the D+T+F mode, Q_R was greatly improved with a high Q_R (>1000 m^3/d) phase (~1000 days). This is because the fractures intensify the hot water injection and provide high-conductive paths for fluid transport [38,39], thereby enlarging the hot water sweep area (Figure 6j–l) and facilitating hydrate decomposition (Figure 5j–l). The final R_D reached 99.5%, 3.98, 2.49, and 2.24 times that in D, D+T, and D+F, respectively. Therefore, hydrate decomposition efficiency is greatly improved by combining thermal stimulation and fracturing.

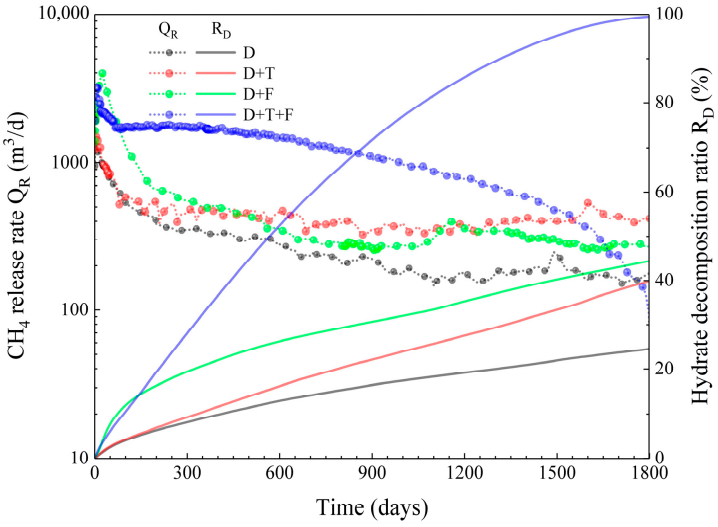

Figure 4. Evolution of Q_R and R_D under different development modes.

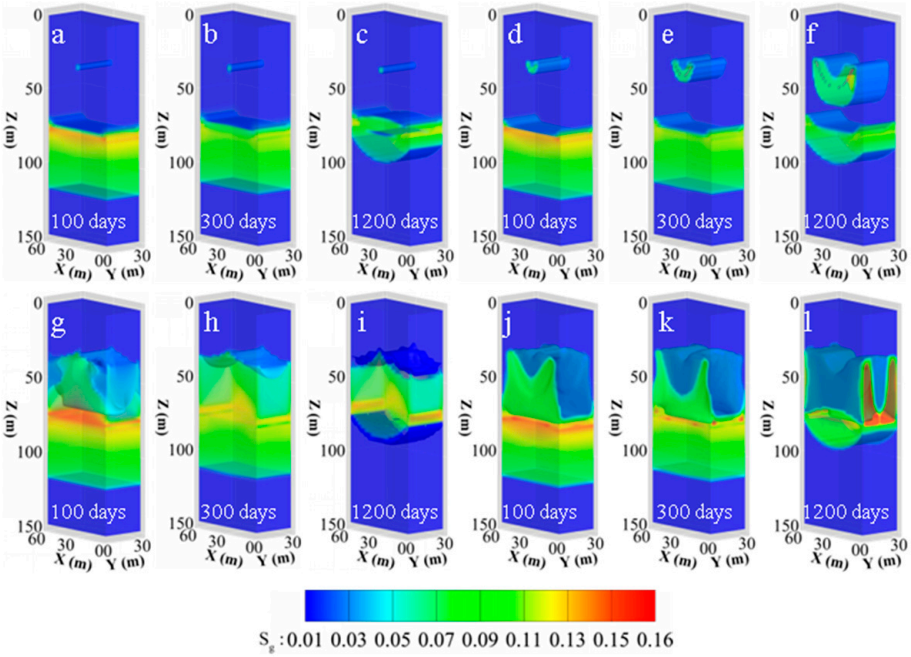

Figure 5. Hydrate distribution in D (**a**–**c**), D+T (**d**–**f**), D+F (**g**–**i**), and D+T+F (**j**–**l**) modes.

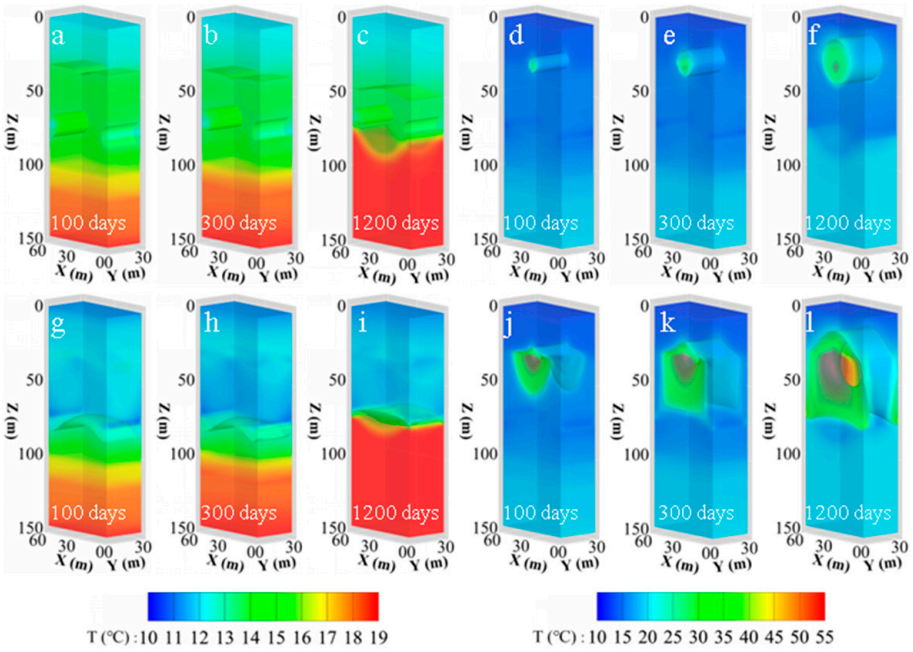

Figure 6. Temperature distribution in D (**a**–**c**), D+T (**d**–**f**), D+F (**g**–**i**), and D+T+F (**j**–**l**) modes.

3.1.2. Gas and Water Production

Figure 7 depicts the evolution of Q_G and V_G under different development modes. Q_G and V_G in the D and D+T modes were almost the same because neither thermal stimulation nor depressurization at the top of the HBL was ineffective. The main gas source layers were the TPL and FGL, with very limited contribution from the HBL (Figure 8a–f). In the D+F mode, Q_G was increased as the decomposition gas was produced (Figure 8g–i), but the stimulation capacity of the fractures was still limited. Unlike the decay of Q_G in the other three scenarios, there was a rise phase (~280 days) after the initial sharp drop of Q_G (Figure 7) due to the contribution of thermal decomposition gas (Figure 8j–l). When the hot water breaks through into the production wells along the fractures (~800 days), Q_G drops dramatically because the hot water in the fracture impedes gas output. The final V_G reached 214 × 10^4 m^3, 2.15, 2.22, and 1.79 times that in the D, D+T, and D+F modes, respectively, suggesting that the D+T+F mode is the most promising.

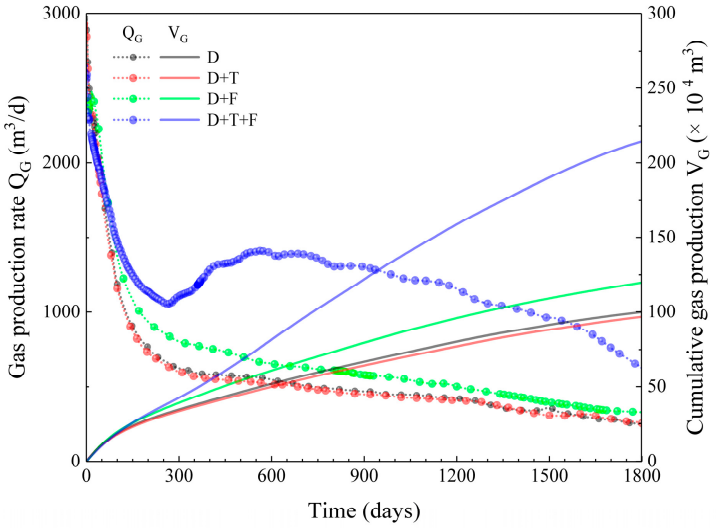

Figure 7. Evolution of Q_G and V_G under different development modes.

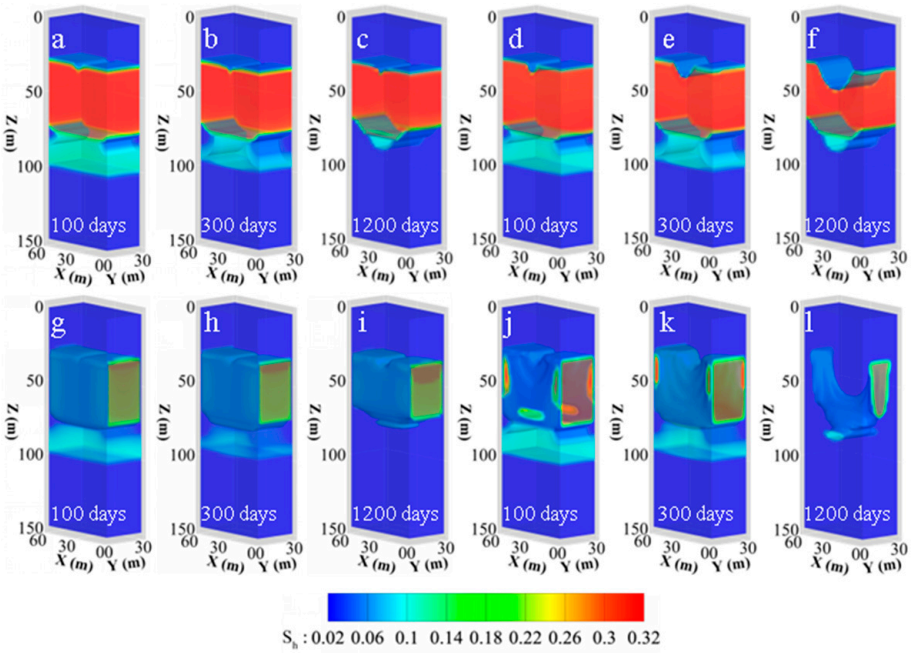

Figure 8. Gas distribution in D (**a**–**c**), D+T (**d**–**f**), D+F (**g**–**i**), and D+T+F (**j**–**l**) modes.

Figure 9 depicts the evolution of V_W and R_{GW} under different development modes. The initial R_{GW} in the D and D+T modes was higher, but afterward, it dropped sharply because of the decreases in Q_G and the increase in V_W. In the D+F mode, the initial R_{GW} was the lowest, while there was an initial increase in R_{GW} due to the stimulation of fractures. The R_{GW} decay rate in the D+T+F mode was the lowest due to the relatively stable Q_G. Overall, when V_G was 130 × 10^4 m^3, the V_W in the D+T+F mode was the lowest, and the corresponding R_{GW} reached 15.72, which was 5.40, 2.69, and 2.61 times that in the D, D+T, and D+F modes, respectively. Consequently, it also manifests the desirable water production performance in the D+T+F mode.

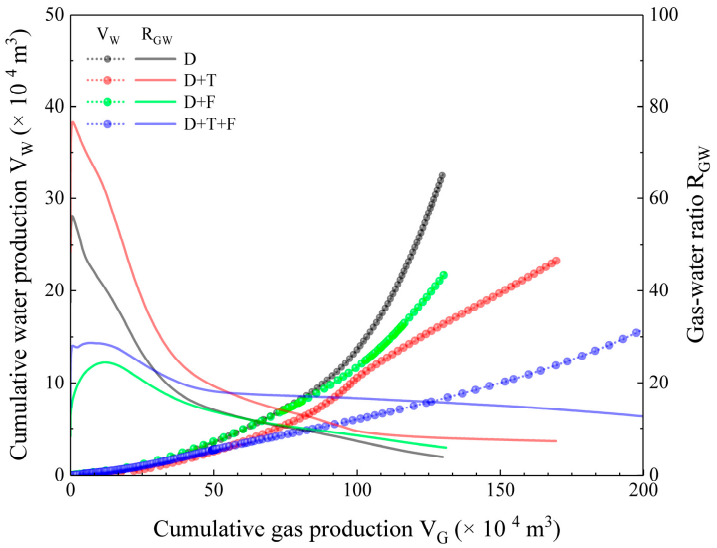

Figure 9. Evolution of V_W and R_{GW} under different development modes.

3.2. *Effect of Fractured Sublayers*

The effect of fractured sublayers was analyzed based on scenario numbers 04~06#.

3.2.1. NGH Dissociation

Figure 10 depicts the evolution of Q_R and R_D under various fractured sublayers. The Q_R in the first 500 days was improved by fracturing the TPL as hydrate dissociation was encouraged in this sublayer (Figure 11a,b), whereas fracturing the FGL hardly affects the Q_R and R_D (Figure 11b,c). Consequently, simultaneous fracturing of the HBL and TPL is a good plan, which can completely decompose the hydrate within 1767 days.

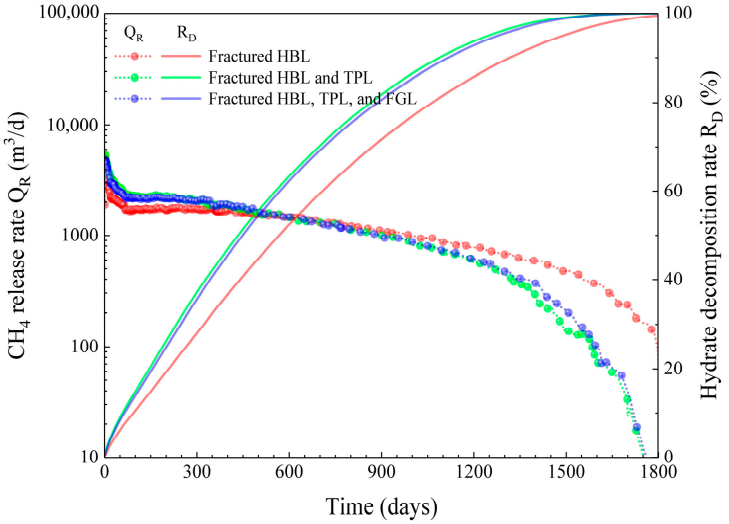

Figure 10. Evolution of Q_R and R_D under various fractured sublayers.

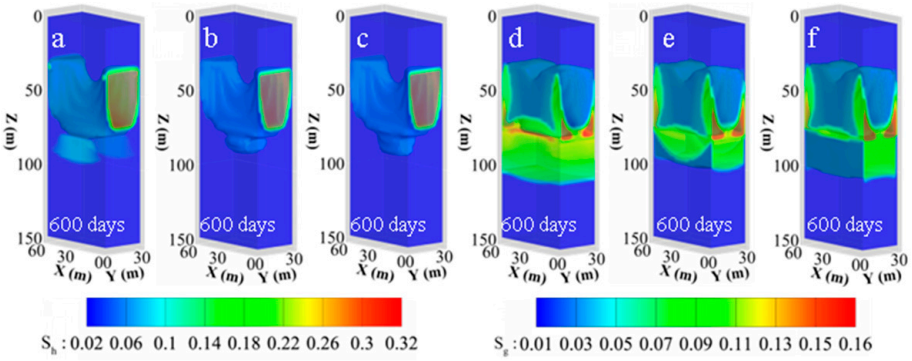

Figure 11. Hydrate and gas distribution in scenario numbers 4 (**a**,**d**), 5 (**b**,**e**), and 6 (**c**,**f**).

3.2.2. Gas and Water Production

Figures 12 and 13 depict the evolution of Q_G, V_G, V_W, and R_{GW} under different fractured sublayers. The initial Q_G increased from 2565 to 3278 m^3/d by fracturing the TPL due to the increased Q_R and the contribution of free gas (Figure 11d,e). Whereas fracturing the FGL reduced Q_G because bottom-water intrusion decreases the gas transport capacity of the fractures (Figure 11e,f). This can also be confirmed by Figure 13, where the final V_W increased from 18 to 21 $\times$ 10^4 m^3 and the final R_{GW} decreased from 10.94 to 9.45 after fracturing the FGL. In addition, the initial R_{GW} was increased after fracturing the TPL and the final R_{GW} was acceptable. As a whole, fracturing the HBL and TPL is the optimal scheme.

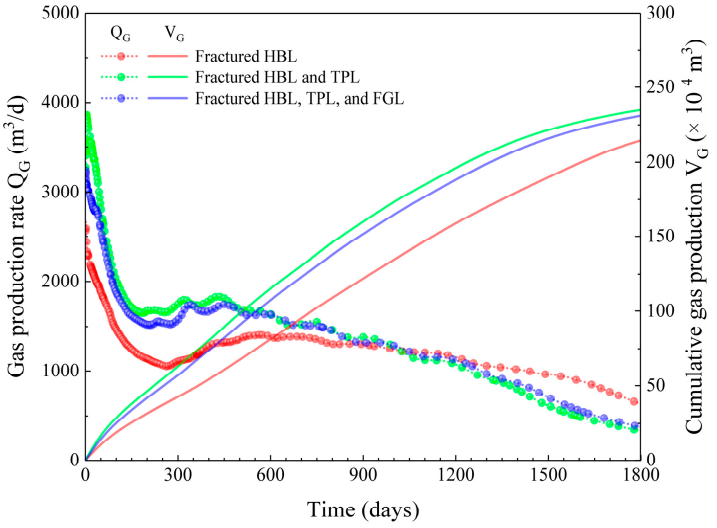

Figure 12. Evolution of Q_G and V_G under different fractured layers.

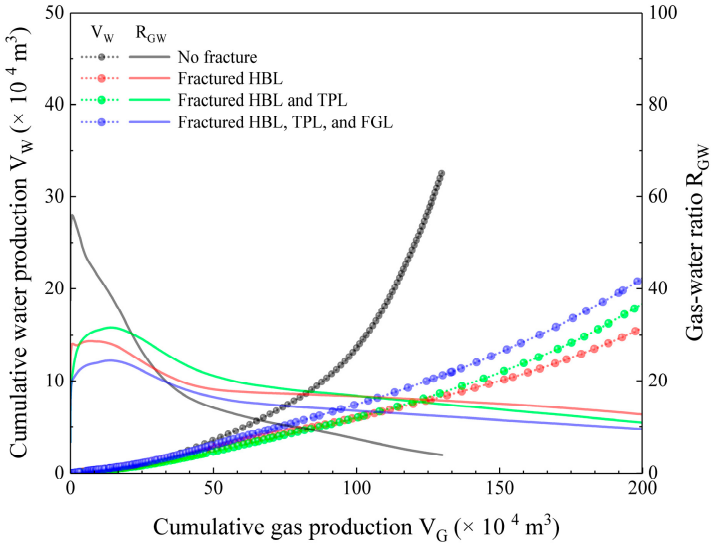

Figure 13. Evolution of V_W and R_{GW} under different fractured layers.

3.3. Effect of Fracture Conductivity and Fracture Spacing

C_F reflects the rate of fluid transport within fractures, while S_F affects the distribution and effective surface area of fractures, and both of them influence fluid migration and production. Therefore, a comparison of the effects of C_F and S_F on co-production dynamics is required to obtain a desirable stimulation scheme. Here, based on scenario numbers 07~11#, 15#, and 19#, the effects of C_F and S_F were analyzed.

3.3.1. NGH Dissociation

Figure 14 depicts the evolution of Q_R and R_D at different C_F and S_F values. The initial Q_R increased from 5132 to 33,797 m^3/d as C_F increased from 10 to 100 D·cm, whereas it was 13,765 m^3/d at an S_F of 5 m, indicating that increasing C_F was more effective. A higher decay rate of Q_R was observed at a higher C_F because of the premature thermal breakthrough [38]. In addition, the enhancement of Q_R was not significant (Figure 15a–d) when C_F was higher than 25 D·cm because of insufficient heat exchange. Different from increasing C_F, the reduction of S_F enhanced heating efficiency due to the increased hot water sweep area, and thus exhibited a higher Q_R (Figure 15e–g). The hydrate dissociation cycle was reduced from 1768 to 1220 days as C_F increased from 10 to 100 D·cm, whereas it

was 645 days at an S_F of 5 m. Consequently, compared with increasing C_F, the decrease in S_F is more effective for hydrate dissociation.

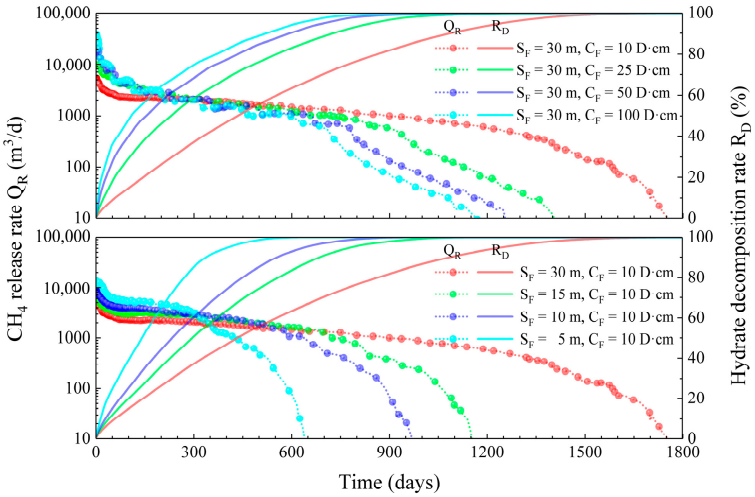

Figure 14. Evolution of Q_R and R_D at different C_F and S_F values.

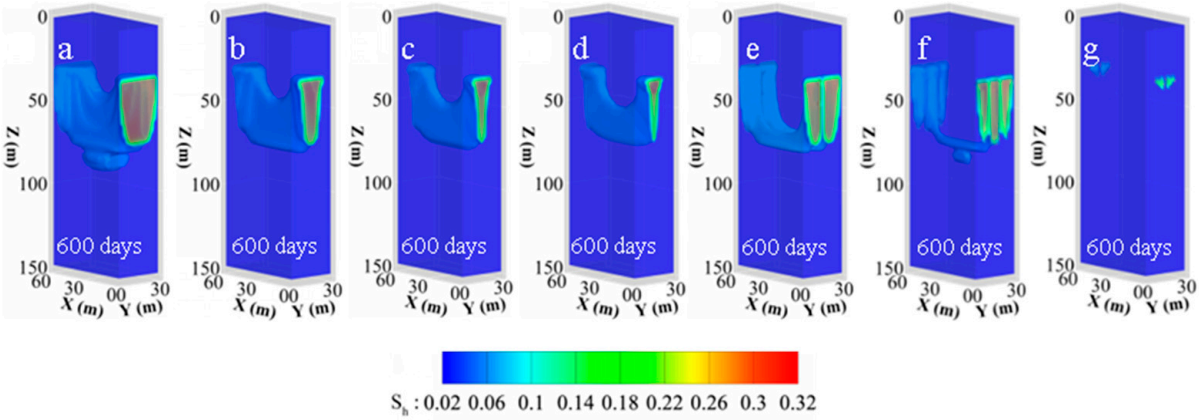

Figure 15. Hydrate distribution: (**a**) S_F = 30 m, C_F = 10 D·cm; (**b**) S_F = 30 m, C_F = 25 D·cm; (**c**) S_F = 30 m, C_F = 50 D·cm; (**d**) S_F = 30 m, C_F = 100 D·cm; (**e**) S_F = 15 m, C_F = 10 D·cm; (**f**) S_F = 10 m, C_F = 10 D·cm; (**g**) S_F = 5 m, C_F = 10 D·cm.

3.3.2. Gas and Water Production

Figures 16 and 17 depict the evolution of Q_G, V_G, V_W, and R_{GW} at different C_F and S_F values. Increasing C_F and S_F mainly increased Q_G in the first 400 days. The difference is that Q_G decreased sharply at higher C_F values, while it was relatively stable at different S_F values. Moreover, V_W increased significantly as C_F increased, while it was barely affected by S_F. Overall, the time and R_{GW} for a V_G of 200×10^4 m^3 was reduced to 550 days and 3.24 as C_F increased to 100 D·cm, whereas they were 535 days and 12.26 at an S_F of 5 m. As a result, both increasing C_F and decreasing S_F help gas recovery, with no increase in water production even at a low S_F value.

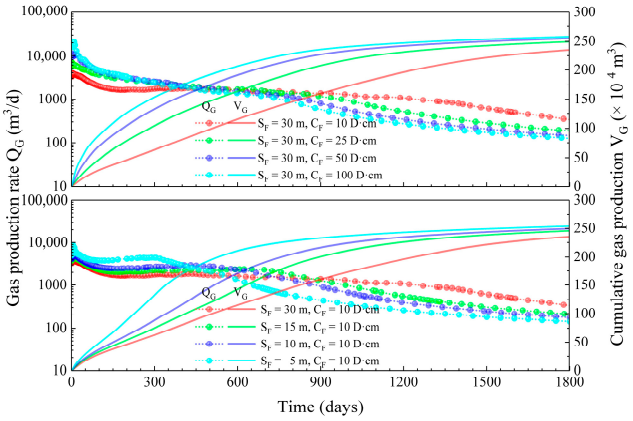

Figure 16. Evolution of Q_G and V_G at different C_F and S_F values.

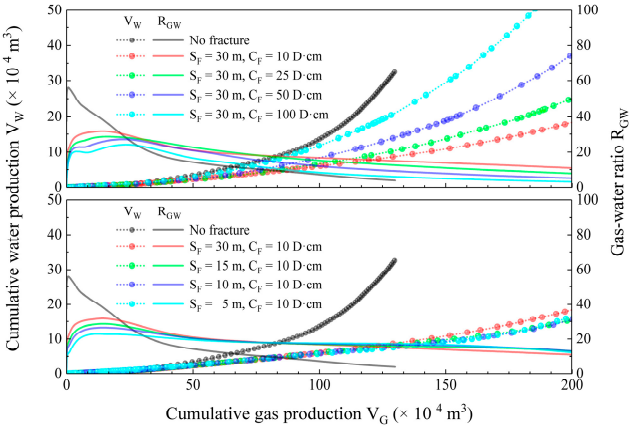

Figure 17. Evolution of V_W and R_{GW} at different C_F and S_F values.

3.4. Vanrican Analysis

Analysis of variance was employed based on the "aov" function in the "R language" (https://www.r-project.org (accessed on 18 June 2022)) to reveal the significance of C_F and S_F and their interactions on co-production performance, and the significance of C_F and S_F to $\overline{Q_R}$, R_{GW}, and $\overline{Q_G}$ are shown in Figure 18. In addition, the main effect and interaction effect were visualized using the "interractionwt" function, as shown in Figure 19.

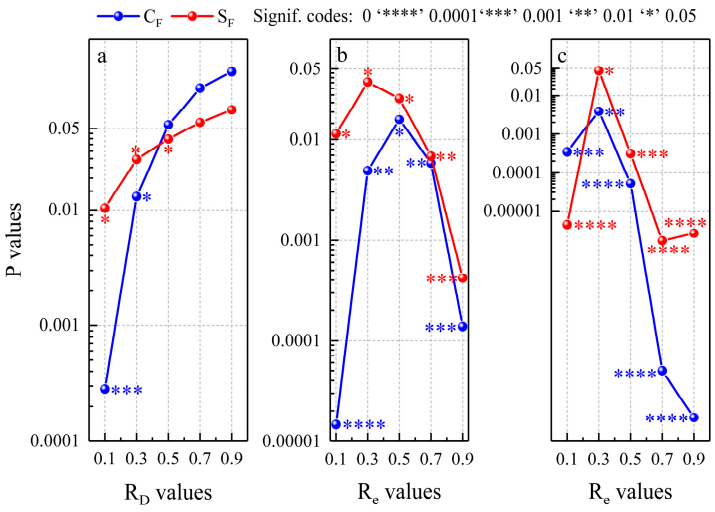

Figure 18. Significance of C_F and S_F to (**a**) $\overline{Q_R}$, (**b**) $\overline{Q_G}$, and (**c**) R_{GW}, in which the *p* value represents the level of significance, and the smaller it is, the more significant the factor is indicated.

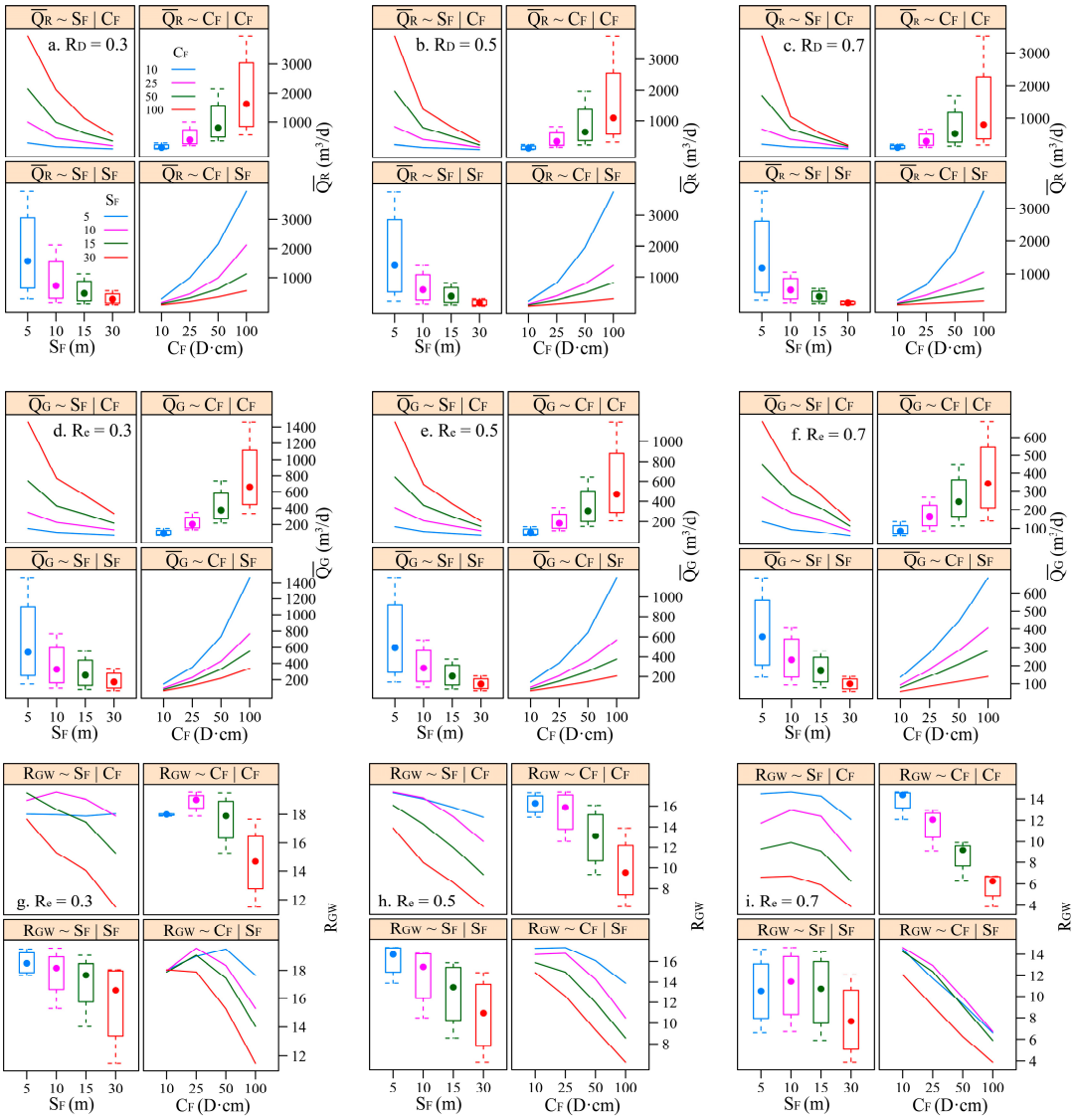

Figure 19. Main (**upper left** and **lower right** subplots) and interaction effects (**upper right** and **lower left** subplots) of C_F and S_F on $\overline{Q_R}$ (**a–c**), $\overline{Q_G}$ (**d–f**), and R_{GW} (**g–i**).

3.4.1. Significance of C_F and S_F to $\overline{Q_R}$

The *p*-values of C_F and S_F in relation to $\overline{Q_R}$ increase as R_D increases (Figure 18a), indicating their significance gradually decreases as production progresses. When R_D was 0.1, C_F was more significant, whereas the significance of S_F was higher when R_D reached 0.5. This indicates that the initial R_D is primarily controlled by C_F, as it directly impacts the rate of fluids (such as gas) flowing through the fractures, thereby greatly affecting the initial gas production rate; and for S_F, its impact on the final R_D is greater because reducing fracture spacing allows for more efficient drainage of the remaining gas, leading to a more significant impact on the final level of reservoir depletion. In addition, C_F has a positive effect on $\overline{Q_R}$ due to the increased hot water flow rate at a lower C_F, while S_F has a negative effect (Figure 19a–c) due to the increased thermal fluid sweep area at a smaller S_F. Therefore, NGH dissociation requires a high C_F and a lower S_F.

3.4.2. Significance of C_F and S_F to $\overline{Q_G}$

The *p*-values of C_F and S_F in relation to $\overline{Q_G}$ first increase and then decrease as R_e increases (Figure 18b). A maximum *p*-value difference occurred at an R_e of 0.1 because the initial gas production was mainly controlled by C_F. When R_e reached 0.4, the signifi-

cance codes of C_F and S_F were the same, suggesting that both C_F and S_F determined the subsequent gas production. The main and interaction effects of C_F and S_F on $\overline{Q_G}$ and $\overline{Q_R}$ were similar (Figure 19a–f). The difference was that their significance to $\overline{Q_G}$ was greater as fractures were the primary channels for gas output. Thus, high-density, high-conductivity fractures are required to enhance co-production efficiency.

3.4.3. Significance of C_F and S_F to R_{GW}

C_F and S_F were significant to R_{GW} at different R_e values (Figure 18c) because both C_F and S_F have a significant impact on gas and water production. When R_e was 0.3, R_{GW} was the highest at a C_F of 25 D·cm and an S_F of 10 m (Figure 19g). Whereas R_{GW} decreased as C_F and S_F increased at an R_e of 0.5, and thus the highest R_{GW} occurred at a C_F of 10 D·cm and an S_F of 5 m (Figure 19h). This is because reducing S_F provides more gas production channels, while lowing C_F reduces the hot water flow rate, thereby increasing gas production and reducing water production. When R_e was 0.7, the ideal R_{GW} can be obtained (Figure 19i) at a C_F of 10 D·cm and an S_F of 5–15 m. In conclusion, if both water control and gas enhancement are considered, one option is to increase the number of fractures but at the same time control the flow capacity of the fractures.

3.5. Commercial Potential Evaluation

Commercial potential evaluation is crucial for the assessment of NGH resources and the design of development plans. According to the experience of two production tests and in conjunction with the economic evaluation, Japan suggests that the $\overline{Q_G}$ of a single well for the industrialized development of marine NGH at least reach 50,000 m^3 [40]. Given further integration with the receptacle R_e value of 0.7 for water-flood development in Chinese offshore gas reservoirs [41], the commercial potential of the proposed development mode was evaluated. Specifically, when the R_e value reaches 0.7, commercial development is possible if the $\overline{Q_G}$ of a single well is higher than 50,000 m^3; otherwise, it is not.

Figure 20 shows the L_W for reaching R_e = 0.7 and $\overline{Q_G}$ = 50,000 m^3. The maximum L_W is 1758 m occurring at a C_F of 10 D·cm and an S_F of 30 m. With the increase of C_F to 100 D·cm and the decrease of S_F to 5 m, it gradually decreases to 146 m. According to the on-site L_W of 250 to 300 m, commercial development of Shenhu hydrates can be realized when C_F is 50 D·cm and S_F = 5 m or when C_F = 100 D·cm and $S_F \leq$ 10 m.

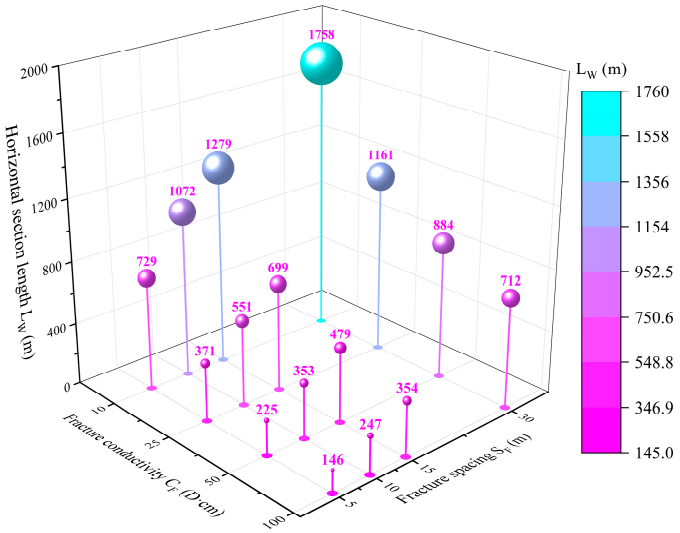

Figure 20. The L_W for reaching R_e = 0.7 and $\overline{Q_G}$ = 50,000 m^3.

4. Conclusions

The co-production potential of multilayered gas hydrate reservoirs using horizontal wells stimulated by hydraulic fracturing and thermal fluid injection was numerically

evaluated, and the influence mechanisms of various factors on co-production behavior were revealed. The following conclusions can be drawn:

1. The stimulation capability of fracturing or thermal fluid injection alone is limited due to severe interlayer contradictions. However, their combination exhibits tantalizing gas production as the inter-well interaction is greatly strengthened by high-conductivity fractures, including promoting pressure drop transmission, enlarging the thermal fluid sweep area, and facilitating fluid injection and gas recovery.

2. Fracturing the HBL and TPL is conducive to hydrate dissociation, while fracturing the FGL induces severe bottom-water intrusion, which greatly increases water production. As a result, fracturing the HBL and TPL simultaneously is recommended.

3. By increasing fracture conductivity and reducing fracture spacing, the hydrate dissociation cycle can be greatly shortened. Moreover, reducing fracture spacing is more effective due to the increased thermal fluid sweep area. As a result, intensive fractures with adequate flow capacity are effective for water control and gas enhancement.

4. The horizontal section length for reaching the commercial development potential is reduced from 1758 to 146 m as the fracture conductivity improved from 10 to 100 D·cm and the fracture spacing reduced from 30 to 5 m, which greatly reduces the exploitation difficulty. Therefore, fractured horizontal wells combined with thermal fluid injection are promising for these multilayered gas hydrate reservoirs.

These findings can provide valuable references for the design of co-production plans and advance the commercialization process of this multilayered gas hydrate reservoir. However, the current simulations were performed under relatively ideal geoengineering conditions due to the lack of sufficient reference data. The inhomogeneous distribution of hydrates, reservoir heterogeneity, and fracture morphology may affect thermal fluid migration, hydrate dissociation, and gas–water flow, resulting in potential biases. Therefore, further research should be conducted on these issues.

Author Contributions: Conceptualization, S.N.; data curation, K.L.; investigation, J.L. and Y.W.; methodology, S.N.; resources, J.L.; software, S.N. and X.Z.; supervision, J.L.; validation, K.L. and Y.W.; writing—original draft, S.N. and X.Z. All authors have read and agreed to the published version of the manuscript.

Funding: This research was funded by Science Research Project of Hebei Education Department, grant number QN2024286.

Institutional Review Board Statement: Not applicable.

Informed Consent Statement: Not applicable.

Data Availability Statement: The data presented in this study are available on request from the corresponding author.

Conflicts of Interest: The authors declare no conflicts of interest.

Nomenclature

M^κ	mass or heat gain term of component κ, kg/m^3 or J/m^3
F^κ	Darcy flux vector of component κ, kg/m^2 or J/m^2
q^κ	mass or heat external yield rate of component κ, kg/m^3/s or W/m^3
$\mathrm{V_n}$	volume of subdomain n, m^3
Γ_n	surface area of subdomain n, m^2
ϕ	porosity, dimensionless
ρ_β	density of phase β, kg/m^3
S_β	saturation of phase β
X_β^κ	mass fraction of component κ in β phase, dimensionless
C_{sed}	heat capacity of dry sediment, J/kg/K
U_β	specific internal energy of phase β, J/kg
E_{dis}	hydrate dissociation activation energy, J/kg
k	intrinsic permeability, m^2

$k_{ir\beta}$	relative permeability of phase β
$S_{ir\beta}$	irreducible saturation of phase β
μ_β	viscosity of phase β, Pa·s
g	gravitational acceleration, 9.806 m/s^2
ω	Klinkenberg factor, Pa
P_β	pressure of phase β, Pa
n_β	stone indexes of phase β
K_{sed}	thermal conductivity of sentiment, W/m/K
ρ_{sed}	sediment density, kg/m^3
K_β	thermal conductivity of phase β, W/m/K
h_β	specific enthalpy of phase β, J/kg
f_σ	radiance emittance factor, dimensionless
σ_0	Stefan–Boltzmann constant, 5:6687 $\times$ 10^8 J/m^2/K^4
P_{cap}	capillary pressure, Pa
P_{the}	threshold pressure, Pa
λ	pore structure index, dimensionless
q_d	direct heat inputs or withdrawals, W/m^3
P_{por}	pore pressure, Pa
P_{atm}	standard atmospheric pressure, 101,325 Pa
ρ_{sw}	seawater density, 1024 kg/m^3
h_0	distance from the seafloor to sea level, m
z	meter below the seafloor, mbsf
T_{sf}	seafloor temperature, K
ΔT	geothermal gradient, K/m
C_F	fracture conductivity, D·cm
S_F	fracture spacing, m
Q_R	CH_4 release rate from NGH dissociation, m^3/d
V_R	cumulative CH_4 release volume from NGH dissociation, m^3
$\overline{Q_R}$	average daily CH_4 release rate, m^3/d
m_D	decomposed hydrate mass, kg
m_H	total hydrate mass in the model, kg
R_D	hydrate decomposition ratio, defined by m_D/m_H, dimensionless
Q_G	gas production rate, m^3/d
V_G	cumulative gas production, m^3
$\overline{Q_G}$	average daily gas production, m^3/d
V_W	cumulative water production, m^3
R_{GW}	gas to water ratio, defined by V_G/V_W, dimensionless
m_R	recovered gas mass, kg
m_G	total gas mass in the model, kg
R_e	timely recovery ratio, defined by m_R/m_G, dimensionless
L_W	horizontal section length, m

References

1. Hubbert, M.K.; Willis, D.G. Mechanics of Hydraulic Fracturing. *Trans. AIME* **1957**, *210*, 153–168. [CrossRef]
2. Chong, Z.R.; Yang, S.H.B.; Babu, P.; Linga, P.; Li, X. Review of natural gas hydrates as an energy resource: Prospects and challenges. *Appl. Energy* **2016**, *162*, 1633–1652. [CrossRef]
3. Hancock, S.; Collett, T.S.; Dallimore, S.R.; Satoh, T.; Inoue, T.; Huenges, E.; Henninges, J.; Weatherill, B. Overview of thermal-stimulation production-test results for the JAPEX/JNOC/GSC et al. Mallik 5L-38 gas hydrate production research wel. In *Scientific Results from the Mallik 2002 Gas Hydrate Production Research Well Program, Mackenzie Delta, Northwest Territories, Canada, (GSC Bulletin; 585), Geological Survey of Canada, CD-ROM*; Dallimore, S.R., Collett, T.S., Eds.; Geological Survey of Canada: Ottawa, ON, Canada, 2005.
4. Boswell, R.; Schoderbek, D.; Collett, T.S.; Ohtsuki, S.; White, M.; Anderson, B.J. The Iġnik Sikumi Field Experiment, Alaska North Slope: Design, Operations, and Implications for CO_2–CH_4 Exchange in Gas Hydrate Reservoirs. *Energy Fuels* **2016**, *31*, 140–153. [CrossRef]
5. Konno, Y.; Fujii, T.; Sato, A.; Akamine, K.; Naiki, M.; Masuda, Y.; Yamamoto, K.; Nagao, J. Key Findings of the World's First Offshore Methane Hydrate Production Test off the Coast of Japan: Toward Future Commercial Production. *Energy Fuels* **2017**, *31*, 2607–2616. [CrossRef]

6. Li, B.; Li, X.; Li, G.; Chen, Z. Evaluation of gas production from Qilian Mountain permafrost hydrate deposits in two-spot horizontal well system. *Cold Reg. Sci. Technol.* **2015**, *109*, 87–98. [CrossRef]
7. Li, J.; Ye, J.; Qin, X.; Qiu, H.; Wu, N.; Lu, H.; Xie, W.; Lu, J.; Peng, F.; Xu, Z.; et al. The first offshore natural gas hydrate production test in South China Sea. *China Geol.* **2018**, *1*, 5–16. [CrossRef]
8. Dai, S.; Santamarina, J.C. *Hydrate-Bearing Clayey Sediments: Morphology, Physical Properties, Production and Engineering/Geological Implications*; Georgia Institute of Technology: Atlanta, GA, USA, 2017. [CrossRef]
9. Guerin, G.; Goldberg, D.; Meltser, A. Characterization of in situ elastic properties of gas hydrate-bearing sediments on the Blake Ridge. *J. Geophys. Res. Solid Earth* **1999**, *104*, 17781–17795. [CrossRef]
10. Zhang, Z.; McConnell, D.R. Seismic modeling analysis and characterization of a gas hydrate and free gas mixed system in Green Canyon, Gulf of Mexico. In Proceedings of the Annual Offshore Technology Conference, Houston, TX, USA, 3 May 2010; Volume 2, pp. 1530–1541.
11. Lee, M.W.; Collett, T.S. Gas hydrate and free gas saturations estimated from velocity logs on Hydrate Ridge offshore Oregon USA. In Proceedings of the Ocean Drilling Program, Scientific Results; Tréhu, A.M., Bohrmann, G., Torres, M.E., Colwell, F.S., Eds.; ODP Publications: CA, USA, 2006; Volume 204, pp. 1–25. Available online: http://www-odp.tamu.edu/publications/204_SR/VOLUME/CHAPTERS/103.PDF (accessed on 18 February 2024).
12. Liang, D.; He, S.; Li, D. Effect of microwave on formation/decomposition of natural gas hydrate. *Sci. Bull.* **2009**, *54*, 965–971. [CrossRef]
13. Minagawa, H.; Ito, T.; Kimura, S.; Kaneko, H.; Noda, S.; Tenma, N. Depressurization and electrical heating of methane hydrate sediment for gas production: Laboratory-scale experiments. *J. Nat. Gas Sci. Eng.* **2018**, *50*, 147–156. [CrossRef]
14. Liang, Y.; Liu, S.; Wan, Q.; Li, B.; Liu, H.; Han, X. Comparison and Optimization of Methane Hydrate Production Process Using Different Methods in a Single Vertical Well. *Energies* **2018**, *12*, 124. [CrossRef]
15. Jin, G.; Xu, T.; Xin, X.; Wei, M.; Liu, C. Numerical evaluation of the methane production from unconfined gas hydrate-bearing sediment by thermal stimulation and depressurization in Shenhu area, South China Sea. *J. Nat. Gas Sci. Eng.* **2016**, *33*, 497–508. [CrossRef]
16. Jin, G.; Peng, Y.; Liu, L.; Su, Z.; Liu, J.; Li, T.; Wu, D. Enhancement of gas production from low-permeability hydrate by radially branched horizontal well: Shenhu Area, South China Sea. *Energy* **2022**, *253*, 124129. [CrossRef]
17. Zhang, J.; Li, X.; Chen, Z.; Li, Q.; Li, G.; Lv, T. Numerical simulation of the improved gas production from low permeability hydrate reservoirs by using an enlarged highly permeable well wall. *J. Pet. Sci. Eng.* **2019**, *183*, 106404. [CrossRef]
18. Feng, Y.; Chen, L.; Suzuki, A.; Kogawa, T.; Okajima, J.; Komiya, A.; Maruyama, S. Enhancement of gas production from methane hydrate reservoirs by the combination of hydraulic fracturing and depressurization method. *Energy Convers. Manag.* **2019**, *184*, 194–204. [CrossRef]
19. Pan, D.; Zhong, X.; Zhu, Y.; Zhai, L.; Zhang, H.; Li, X.; Wang, Y.; Chen, C. CH_4 recovery and CO_2 sequestration from hydrate-bearing clayey sediments via CO_2/N_2 injection. *J. Nat. Gas Sci. Eng.* **2020**, *83*, 103503. [CrossRef]
20. Ma, Y.; Zhong, X.; Li, X.; Nie, S.; Li, Q.; Tu, G.; Chen, C. Numerical simulation of gas extraction from marine hydrate sediments using sodium chloride injection. *Fuel* **2023**, *342*, 127910. [CrossRef]
21. Chen, C.; Meng, Y.; Zhong, X.; Nie, S.; Ma, Y.; Pan, D.; Liu, K.; Li, X.; Gao, S. Research on the Influence of Injection–Production Parameters on Challenging Natural Gas Hydrate Exploitation Using Depressurization Combined with Thermal Injection Stimulated by Hydraulic Fracturing. *Energy Fuels* **2021**, *35*, 15589–15606. [CrossRef]
22. Jin, Y.; Li, S.; Yang, D.; Jiang, X. Determination of dissociation front and operational optimization for hydrate development by combining depressurization and hot brine stimulation. *J. Nat. Gas Sci. Eng.* **2018**, *50*, 215–230. [CrossRef]
23. Yu, T.; Guan, G.; Wang, D.; Song, Y.; Abudula, A. Numerical evaluation on the effect of horizontal-well systems on the long-term gas hydrate production behavior at the second Shenhu test site. *J. Nat. Gas Sci. Eng.* **2021**, *95*, 104200. [CrossRef]
24. Yu, T.; Guan, G.; Wang, D.; Song, Y.; Abudula, A. Gas Production Enhancement from a Multilayered Hydrate Reservoir in the South China Sea by Hydraulic Fracturing. *Energy Fuels* **2021**, *35*, 12104–12118. [CrossRef]
25. Ma, X.; Sun, Y.; Guo, W.; Jia, R.; Li, B. Numerical simulation of horizontal well hydraulic fracturing technology for gas production from hydrate reservoir. *Appl. Ocean Res.* **2021**, *112*, 102674. [CrossRef]
26. Yin, F.; Gao, Y.; Chen, Y.; Sun, B.; Li, S.; Zhao, D. Numerical investigation on the long-term production behavior of horizontal well at the gas hydrate production site in South China Sea. *Appl. Energy* **2022**, *311*, 118603. [CrossRef]
27. Guo, K.; Fan, S.; Wang, Y.; Lang, X.; Zhang, W.; Li, Y. Physical and chemical characteristics analysis of hydrate samples from northern South China sea. *J. Nat. Gas Sci. Eng.* **2020**, *81*, 103476. [CrossRef]
28. Qin, X.; Lu, J.; Lu, H.; Qiu, H.; Liang, J.; Kang, D.; Zhan, L.; Lu, H.; Kuang, Z. Coexistence of natural gas hydrate, free gas and water in the gas hydrate system in the Shenhu Area, South China Sea. *China Geol.* **2020**, *3*, 210–220. [CrossRef]
29. Moridis, G.J.; Sloan, E.D. Gas production potential of disperse low-saturation hydrate accumulations in oceanic sediments. *Energy Convers. Manag.* **2007**, *48*, 1834–1849. [CrossRef]
30. Chen, L.; Feng, Y.; Okajima, J.; Komiya, A.; Maruyama, S. Production behavior and numerical analysis for 2017 methane hydrate extraction test of Shenhu, South China Sea. *J. Nat. Gas Sci. Eng.* **2018**, *53*, 55–66. [CrossRef]
31. Moridis, G.J. Numerical Studies of Gas Production from Methane Hydrates. *SPE J.* **2003**, *8*, 359–370. [CrossRef]
32. Stone, H.L. Probability Model for Estimating Three-Phase Relative Permeability. *J. Pet. Technol.* **1970**, *22*, 214–218. [CrossRef]
33. Makogon, Y.F. Natural gas hydrates—A promising source of energy. *J. Nat. Gas Sci. Eng.* **2010**, *2*, 49–59. [CrossRef]

34. Ye, J.; Qin, X.; Xie, W.; Lu, H.; Ma, B.; Qiu, H.; Liang, J.; Lu, J.; Kuang, Z.; Lu, C.; et al. The second natural gas hydrate production test in the South China Sea. *China Geol.* **2020**, *3*, 197–209. [CrossRef]
35. Sun, J.; Ning, F.; Li, S.; Zhang, K.; Liu, T.; Zhang, L.; Jiang, G.; Wu, N. Numerical simulation of gas production from hydrate-bearing sediments in the Shenhu area by depressurising: The effect of burden permeability. *J. Unconv. Oil Gas Resour.* **2015**, *12*, 23–33. [CrossRef]
36. Gao, Y.; Yang, M.; Zheng, J.; Chen, B. Production characteristics of two class water-excess methane hydrate deposits during depressurization. *Fuel* **2018**, *232*, 99–107. [CrossRef]
37. Ahmadi, G.; Ji, C.; Smith, D.H. Production of natural gas from methane hydrate by a constant downhole pressure well. *Energy Convers. Manag.* **2007**, *48*, 2053–2068. [CrossRef]
38. Zhong, X.; Pan, D.; Zhai, L.; Zhu, Y.; Zhang, H.; Zhang, Y.; Wang, Y.; Li, X.; Chen, C. Evaluation of the gas production enhancement effect of hydraulic fracturing on combining depressurization with thermal stimulation from challenging ocean hydrate reservoirs. *J. Nat. Gas Sci. Eng.* **2020**, *83*, 103621. [CrossRef]
39. Ju, X.; Liu, F.; Fu, P.; White, M.D.; Settgast, R.R.; Morris, J.P. Gas Production from Hot Water Circulation through Hydraulic Fractures in Methane Hydrate-Bearing Sediments: THC-Coupled Simulation of Production Mechanisms. *Energy Fuels* **2020**, *34*, 4448–4465. [CrossRef]
40. Research Consortium for Methane Hydrate Resources in Japan. 2017. Available online: https://www.mh21japan.gr.jp/mh21wp/wp-content/uploads/mh21form2017_doc01.pdf (accessed on 29 November 2017).
41. Li, Z. *Basic Theory and Technology of Waterflooding Oilfield Development*; Science Press Beijing: Beijing, China, 2019; pp. 68–70.